The Astrophysical Journal, 889:147 (13pp), 2020 February 1 https://doi.org/10.3847/1538-4357/ab6327

The Stark Effect, Zeeman Effect, and Transition Dipole Moments for the $B^2\Sigma^+-X^2\Sigma^+$ Band of Aluminum Monoxide, AlO

Xilin Bai and Timothy C. Steimle
School of Molecular Science Arizona State University Tempe, AZ 85287, USA; TSteimle@asu.edu
Received 2019 October 23; revised 2019 December 3; accepted 2019 December 16; published 2020 February 3

Abstract

The experimentally measured radiative lifetimes and branching ratios were combined to determine the transition dipole moments for the $B^2\Sigma^+(v=0–3) \rightarrow X^2\Sigma^+(v=0–6)$ bands of aluminum monoxide, AlO, and compared with theoretical predictions. The $B^2\Sigma^+$–$X^2\Sigma^+$ (0, 1) band of a molecular beam sample of AlO was recorded at high spectral resolution both field-free and in the presence of static electric and magnetic fields. The ^{27}Al($I=5/2$) hyperfine interaction in the $B^2\Sigma^+(v=0)$ state was analyzed. The observed Stark shifts were analyzed to produce permanent electric dipole moments of 1.94(8) D and 4.45(3) D for the $B^2\Sigma^+(v=0)$ and $X^2\Sigma^+(v=1)$ states, respectively. It is demonstrated that the observed Zeeman spectra can be simulated using an effective Hamiltonian with the associated expected g-factors for both the $X^2\Sigma^+(v=1)$ and $B^2\Sigma^+(v=0)$ states.

Unified Astronomy Thesaurus concepts: Molecular spectroscopy (2095); Line intensities (2084); Transition probabilities (2074); Magnetic fields (994); Circumstellar dust (236); Circumstellar clouds (234); Circumstellar gas (238); Radio astronomy (1338)

1. Introduction

The relevance of rotational and optical spectroscopy of gas-phase aluminum monoxide, AlO, to astronomy is well documented (Patrascu et al. 2015). The relevance to astronomy stems from the fact that the readily detected AlO is a direct gas-phase precursor of alumina dust, Al_2O_3 (s) (Gobrecht et al. 2015; Sarangi & Cherchneff 2015), which is difficult to directly detect. Specifically, broad emission in the 11–12 μm wavelength range observed for many oxygen-rich asymptotic giant branch stars is generally believed to be from aluminum oxide (Al_2O_3) dust (Ishizuka et al. 2018). The poorly understood chemical synthesis of dust is generally believed to be initiated by a series of gas-phase chemical reactions involving small molecules. In the case of alumina formation, it is postulated that molecular Al_2O_3 is formed by the dimerization of AlO, followed by the oxidation of the dimer (Biscaro & Cherchneff 2016). Subsequently, the dimer $(Al_2O_3)_2$ is formed and serves as the stable gas phase seed for alumina dust formation (Gobrecht et al. 2015). The pure rotational transitions of AlO in the $X^2\Sigma^+(v=0)$ state have been used for the detection of AlO in the vicinity of the oxygen-rich red supergiant VY Canis Majoras (Tenenbaum & Ziurys 2009), the Mira variable stars *o* Ceti (Kaminski et al. 2016), R Aquarii (De Beck et al. 2017), and W Hydrae (Takigawa et al. 2017). The visible $B^2\Sigma^+$–$X^2\Sigma^+$ transition has also been observed in both absorption and emission in the vicinity of Mira variable *o* Ceti (Kaminski et al. 2016). Both the visible and millimeter wave spectra of AlO exhibit complex spatial and temporal variations in Mira variable *o* Ceti (Kaminski et al. 2016), as does the infrared spectral features associated with dust (Lobel et al. 2000) around this source making the spectroscopy of AlO a venue for understanding the physical and chemical forces behind dust formation. Transformation of both the visible and millimeter-wave astrophysical spectral intensities to column densities requires experimental determinations of transition dipole moments (TDMs).

Here we report on the experimental determination of the transition dipole moments TDMs for the $B^2\Sigma^+(v=0–3) \rightarrow X^2\Sigma^+(v=0–6)$ transitions from a combined analysis of the radiative lifetimes and branching ratios recorded using medium resolution laser-induced fluorescence (LIF) spectroscopy of a supersonic free-jet sample. In addition, the permanent electric dipole moments and magnetic g-factors for the $B^2\Sigma^+(v=0)$ and $X^2\Sigma^+(v=1)$ states, and the ^{27}Al($I=5/2$) hyperfine parameters for the $B^2\Sigma^+(v=0)$ state were determined from the analyses of high-resolution optical field-free, Stark and Zeeman spectra of a cold molecular beam sample. The determined permanent electric dipole moment for the $X^2\Sigma^+$ state will assist in conversion of rotational transition intensities to column densities.

Although the laboratory spectrum of the $B^2\Sigma^+$–$X^2\Sigma^+$ band system has been extensively studied (Lagerqvist et al. 1957; Johnson et al. 1972; Dagdigian et al. 1975; Hebert et al. 1980; Coxon & Naxakis 1985; Kraus et al. 2002; Saksena et al. 2008; Launila & Berg 2011), to the best of our knowledge, the work reported here is the only high-resolution (i.e., near natural linewidth limit) optical spectroscopic study of a molecular beam sample of AlO. The field-free energy levels of the $X^2\Sigma^+$, $A^2\Pi_i$, and $B^2\Sigma^+$ states of AlO are well characterized due to the analysis of the pure rotational spectrum of the $X^2\Sigma^+$ state (Toerring & Herrmann 1989; Yamada et al. 1990; Goto et al. 1994; Breier et al. 2018) and the combined analysis of the Doppler limited resolution spectra of the $A^2\Pi_i$–$X^2\Sigma^+$ and $B^2\Sigma^+$–$X^2\Sigma^+$ electronic transitions (Launila & Berg 2011). There are no previous reports of Stark and Zeeman spectroscopy of AlO. Although the ^{27}Al($I=5/2$) hyperfine interactions in the $X^2\Sigma^+$ state are well characterized from the analysis of the pure rotational spectrum (Toerring & Herrmann 1989; Yamada et al. 1990; Goto et al. 1994; Breier et al. 2018), the hyperfine interaction for the $B^2\Sigma^+$ state has not been precisely determined. An estimate of the hyperfine interaction parameters for the $B^2\Sigma^+$ state based upon observed line broadening has been reported (Launila & Berg 2011).

There have been numerous theoretical predictions for the properties of AlO (Yoshimine et al. 1973; Lengsfield & Liu 1982; Partridge et al. 1983; Zenouda et al. 1999;

Honjou 2010; Patrascu et al. 2014, 2015; Feng & Zhu 2019), including molecular frame permanent electric dipole moments, $\boldsymbol{\mu}_{el}$, and electric TDMs, $\mu_{iv',fv''}$. The most relevant theoretical study for the measurements performed here is the ab initio prediction of a comprehensive set of transition frequencies and accurate transition intensities involving the $X^2\Sigma^+$, $A^2\Pi_i$, and $B^2\Sigma^+$ states carried out as part of the ExoMol project (Patrascu et al. 2015). An extensive catalog ($>2\times10^7$ lines) of the transition frequencies and Einstein A-coefficients for the $^{27}Al^{16}O$,$^{27}Al^{18}O$, $^{27}Al^{17}O$, and $^{26}Al^{16}O$ isotopologues spanning frequencies up to 35,000 cm^{-1} was produced. The calculated electric dipole moment curves predict $\boldsymbol{\mu}_{el}$ values of 4.39 D and 2.18 D for the $X^2\Sigma^+$ and $B^2\Sigma^+$ states and a TDM for the $B^2\Sigma^+ \rightarrow X^2\Sigma^+$ transition of 1.85 D at an internuclear separation of 1.76 Å. A comparison to previously measured radiative fluorescent lifetimes (Johnson et al. 1972; Dagdigian et al. 1975) of individual excited $B^2\Sigma^+$ vibronic levels, $\tau_{iv'}$, was used as a metric for gauging the reliability of the ab initio predictions (Patrascu et al. 2015) due to the lack of experimental values for $\mu_{iv',fv''}$ and $\boldsymbol{\mu}_{el}$. The fidelity of a comparison of experimental and theoretical $\tau_{iv'}$ values is low because the two reported (Johnson et al. 1972; Dagdigian et al. 1975) sets of experimental values, both of which were determined more than 45 yr ago, do not agree within the stated error limits. Specifically, $\tau_{iv'}$ for the $v=0$, 1, and 2 vibrational levels of the $B^2\Sigma^+$ state have been measured to be 128.6 ± 6, 125.5 ± 2.6, and 130.5 ± 7 ns, respectively, by Johnson et al. (1972) and to be 100 ± 7, 102 ± 7, and 102 ± 4 ns, by Dagdigian et al. (1975). The recent ExoMol project ab initio prediction gives values of 92.4, 94.5, and 96.7 ns, respectively, while a prediction reported some time ago (Partridge et al. 1983) gives 109.9, 112.6, and 115.2 ns, respectively. A very recent prediction (Feng & Zhu 2019) gives 233, 235, and 236 ns. One goal of the present study is to precisely determine $\tau_{iv'}$ values by implementing technology that was not available when the two previous measurements were performed.

Unlike the extensive experimental investigations into the energies and related spectroscopic parameters, there have been relatively few experimental studies of the transition intensities for AlO. Some time ago the relative values of the electronic transition moment as a function of bond length, R_e (R), were experimentally determined (Sato et al. 1995) from analysis of the relative intensity of the $B^2\Sigma^+(v=0,$ 1, and 2) $\rightarrow X^2\Sigma^+(v=0,$ 1, 2, 3, and 4) emission. In that study, a hot sample of AlO was generated using a microwave discharge source and the data involved relatively high rotational levels ($N' = 19$–32). Also many years ago the absolute band strengths of the $B^2\Sigma^+$–$X^2\Sigma^+$ electronic transition were reported (Hebert et al. 1980). In that study the experimentally derived relative transition probabilities obtained from the analysis of low-resolution emission spectra (Linton & Nicholls 1969) were combined with the $\tau_{iv'}$ values from Dagdigian et al. (1975) to determine rotationally averaged Einstein A-coefficients, $A_{iv',fv''}$ (see below). The method employed (Hebert et al. 1980) for transforming from relative to absolute intensities required calculating r-centroids and Franck–Condon factors from an assumed precise set of potential energy curves.

An assessment of the ab initio predicted TDMs (Patrascu et al. 2015) was recently performed as part of a laboratory kinetics study of the formation of AlO (Gomez Martin et al. 2017). As part of that study the measured rotationally resolved absorption cross-section, $\sigma_{v'J',v''J''}(\tilde{\nu})$, at the bandhead of the $B^2\Sigma^+(v=0)\leftarrow X^2\Sigma^+(v=0)$ system was determined (Gomez Martin et al. 2017) to be $(6.7\pm1.6)\times10^{-15}$ cm^2 per molecule. To validate this experimentally determined value, a comparison of simulated and observed rotationally resolved LIF spectra was made. Specifically, known molecular constants (Launila & Berg 2011) were used to generate RKR1 potentials that were in turn used to generate numerical vibrational wavefunctions. These wavefunctions were then combined with the ab initio predicted TDM curves (Patrascu et al. 2015) and used to compute synthetic spectra using the PGOPHER spectral simulator (Western 2017). The observed LIF excitation spectrum at the $B^2\Sigma^+$–$X^2\Sigma^+$ (0, 0) bandhead obtained using the ab initio TDM curves (Patrascu et al. 2015) predicted $\sigma_{v'J',v''J''}(\tilde{\nu})$ of 8.5×10^{-15} cm^2 per molecule, which was considered to be in good agreement with the measured value of $(6.7\pm1.6)\times10^{-15}$ cm^2 $molecule^{-1}$.

Here a more direct method of determining vibronic TDMs, $\mu_{iv',fv''}$, via a combination of precisely measured radiative lifetimes, $\tau_{iv'}$, and fluorescence branching ratios, $b_{iv',fv''}$, is reported and are compared to $\mu_{iv',fv''}$ values extracted from the calculated (Patrascu et al. 2015) Einstein A-coefficient, $A_{v'J',v''J''}$. The $A_{v'J',v''J''}$ values describe the first order rate coefficient for spontaneous emission from the excited rovibronic levels, v', J', to the ground and low-lying rovibronic v'', J'' levels, each having a transition frequency $\tilde{\nu}_{v'J',v''J''}$. $A_{v'J',v''J''}$ is given by (Hansson & Watson 2005):

$$A_{v'J',v''J''} = 3.136\times10^{-7}\times\frac{\tilde{\nu}^3_{v'J',v''J''}S_{v'J',v''J''}}{(2J'+1)}, \quad (1)$$

where the line strength factor, $S_{v'J',v''J''}$, is proportional to the square of the TMD. The numerical coefficient of Equation (1) assumes units of Debye (D) and wavenumbers (cm^{-1}). In the present dispersed fluorescence intensity measurements, the rotational fine structure is not resolved and the summation over the line strength factors gives:

$$A_{iv',fv''} = 3.136\times10^{-7}\,|\mu_{iv',fv''}|^2\tilde{\nu}^3_{iv',fv''} = b_{iv',fv''}\tau^{-1}_{iv'} \quad (2)$$

where $\mu_{iv',fv''}$ is the vibronic TDM and $b_{iv',fv''}$ is the fluorescence branching ratio. The experimental value for the magnitude of the vibronic TDMs are obtained using the experimentally measured $b_{iv',fv''}$ and $\tau_{iv'}$ values in conjunction with Equation (2).

2. Experimental

Numerous types of spectroscopic measurements, all using LIF detection, were performed; medium resolution ($\Delta\tilde{\nu}\sim0.1$ cm^{-1}) broad survey scans and associated dispersed LIF (DLIF), and high-resolution ($\Delta\tilde{\nu}\sim0.0003$ cm^{-1}) laser excitation spectroscopy. The medium resolution measurements were performed on a free-jet expansion sample, whereas, the high-resolution measurements on a well-collimated molecular beam. The high-resolution LIF spectra were recorded both field-free and in the presence of static electric (optical Stark) and magnetic (optical Zeeman) fields. The rotationally cold ($T^{rot.}\sim20$ K) AlO sample was generated by laser ablation of a continuously rotating aluminum metal rod in a supersonic expansion of approximately 5% N_2O gas mixture seeded in either argon or helium at a stagnation pressure of ~2 MPa. A vibrational warmer sample was achieved using helium, which facilitated the studies involving $X^2\Sigma^+(v>0)$ states. The faster

beam associated with helium also resulted in less radiative relaxation to the ground vibrational level as the sample traversed the 0.5 m separation between the ablation source and the probe region of the high-resolution spectrometer.

Initial detection was achieved by performing pulsed dye laser survey scans using a two-dimensional (2D) spectroscopic technique (Reilly et al. 2006) in the 20,100–21,600 cm^{-1} and 19,200–19,700 cm^{-1} spectral ranges associated with the $\Delta v = 0$ and $\Delta v = -1$ bands of the $B^2\Sigma^+$–$X^2\Sigma^+$ electronic transition. The 2D spectra are created by stepping the pulsed dye laser wavelength and capturing a 75 nm wide spectral region of the dispersed laser-induced fluorescence as viewed through a 2/3 m, low f-number (=4.1), monochromator. A cooled, gated, intensified charge coupled detector (ICCD) was attached to the monochromator. Typically, 20 laser ablation samples were averaged at each pulsed dye laser wavelength and a 1 μs detection window used for the ICCD. In our implementation of the 2D technique (Kokkin et al. 2014) the center wavelength of monochromator is tracked with the laser excitation wavelength. The 2D spectrum was subsequently processed to produce medium resolution excitation spectra and DLIF spectra by vertically summing the signal in a horizontal slice and horizontally summing the signal in a vertical slice, respectively (see below). The entrance slit width of the monochromator was typically set to 2 mm resulting in an approximately ± 4 nm a spectral resolution for the DLIF signal of the 2D spectra. Higher resolution DLIF were subsequently recorded by tuning the pulsed dye laser wavelength to a resonate wavelength and narrowing the entrance slit of the monochromator to approximately 0.3 mm. Typically 10,000 laser ablation samples were averaged for the higher resolution DLIF spectroscopy. The relative sensitivity of the spectrometer as a function of wavelength was calibrated using a blackbody radiation source. Wavelength calibration of the DLIF spectra was achieved by recording the emission of an argon pen lamp. Fluorescent lifetime measurements of the $B^2\Sigma^+(v = 0–3)$ levels were performed by tuning the wavelength of the pulsed dye laser to the intense R_1-branch heads of the $\Delta v = 0$ and $\Delta v = -1$ bands of the $B^2\Sigma^+$–$X^2\Sigma^+$ electronic transition and monitoring the DLIF spectrum with a relatively wide (1 μs) ICCD detection window. The detection window was progressively stepped further in time from the incident pulsed laser in 10 ns increments. The resulting fluorescence decay curves were fit to a first order exponential to determine the upper state fluorescence lifetimes $\tau_{iv'}$.

High-resolution, field-free (FF), optical Stark, and optical Zeeman excitation spectra were recorded for the $B^2\Sigma^+$–$X^2\Sigma^+$ (0, 1) band near 508.2 nm. The $B^2\Sigma^+$–$X^2\Sigma^+$(0, 0) band near 485.1 nm is outside the operating range of our continuous wave (cw) dye laser. For these measurements the free-jet expansion was skimmed to produce a well-collimated molecular beam which was probed approximately 0.5 m from the ablation source with the output of a tunable, cw-dye laser. The excitation spectra for the $B^2\Sigma^+$–$X^2\Sigma^+$ (0, 1) band was recorded by viewing the off-resonance $B^2\Sigma^+(v = 0) \rightarrow X^2\Sigma^+(v = 0)$ emission through a 490 ± 10 nm bandpass filter and processed using gated photon counting techniques. For the Stark measurements, static electric fields were generated by application of a voltage across a pair of highly transmitting, conducting, neutral density filters. For the Zeeman measurements, static magnetic fields were generated using rare earth magnets attached to an iron yoke. A polarization rotator was

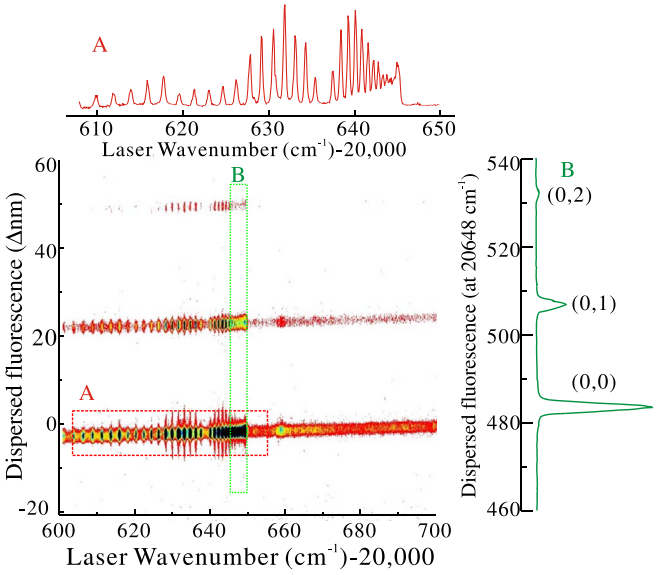

Figure 1. The 2D spectrum of the products of an ablated Al/N_2O supersonic expansion in the 20,600–20,700 cm^{-1} spectral range. The horizontal axis is the laser excitation wavenumber and the vertical axis is the dispersed laser-induced fluoresce (DLIF) wavelength relative to the laser excitation wavelength. The 75 nm spectral window of the DLIF is tracked with the laser excitation wavelength. The spectrum at the top is the medium resolution $X^2\Sigma^+(v = 0) \rightarrow B^2\Sigma^+(v = 0)$ LIF excitation spectrum obtained by vertical integration of the indicated horizontal slice centered on the laser wavelength (i.e., on-resonance detection). The spectrum on the right is the low-resolution DLIF spectrum obtained by horizontal integration of the indicated vertical rectangular slice centered at the $B^2\Sigma^+$–$X^2\Sigma^+$ (0, 0) bandhead ($\nu = 20{,}648$ cm^{-1}).

used to align the electric field vector of the linearly polarized laser radiation either parallel "∥" or perpendicular "⊥" to that of the applied electric or magnetic field or electric field vector. The systematic errors due to field strength calibration were estimated to be less than 2%. Typically, the photon counts of 30 laser ablation pulses were coadded at a given cw-dye laser excitation wavelength. There are no convenient wavelength calibrated spectra in this spectral range, equivalent sub-Doppler absorption spectrum of I_2 that is often used for cw-laser calibration at longer wavelengths. Accordingly, the absolute wavenumber of the cw-dye laser was determined to ±0.001 cm^{-1} using a commercial wavemeter. The relative wavenumber of the spectral features were precisely measured (±0.0003 cm^{-1}) by simultaneously corecording the transmissions of an actively stabilized and calibrated étalon (free spectra range (fsr) = 754.244 MHz).

3. Observations

The 2D spectrum of the products of an ablated $Al/5\%N_2O/95\%He$ supersonic expansion of the $\Delta v = 0$ bands in the 20,600–20,700 cm^{-1} spectral range is presented in Figure 1. At the top is the medium resolution $X^2\Sigma^+(v = 0) \rightarrow B^2\Sigma^+(v = 0)$ LIF excitation spectrum obtained by vertical integration of the indicated horizontal slice centered on the laser wavelength (i.e., on-resonance detection). The spectrum on the right is the medium resolution DLIF spectrum obtained by horizontal integration of the vertical rectangular slice centered at the $B^2\Sigma^+$–$X^2\Sigma^+$ (0, 0) bandhead ($\tilde{\nu} = 20{,}648$ cm^{-1}). The 2D spectrum of the $\Delta v = -1$ bands in the 19,550–19,685 cm^{-1}spectral range is presented in Figure 2. The medium resolution $X^2\Sigma^+(v = 1, 2) \rightarrow B^2\Sigma^+(v = 0, 1)$ LIF excitation spectrum obtained by vertical integration of the

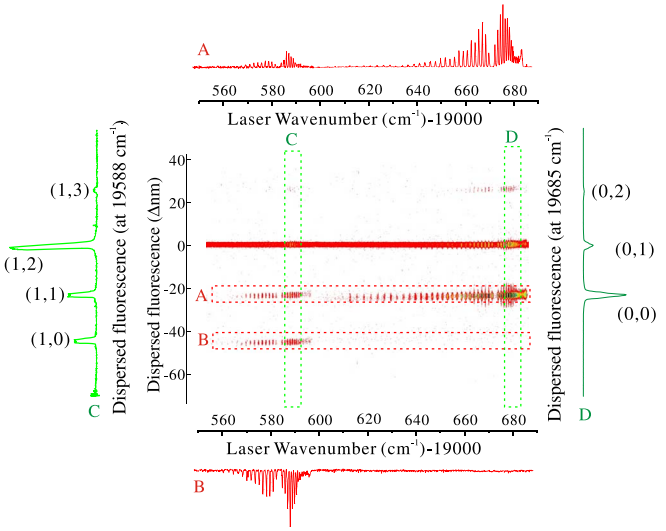

Figure 2. The 2D spectrum of the $\Delta v = -1$ bands in the 19,550 to 19,685 cm^{-1} spectral range. At the top is the medium resolution $X^2\Sigma^+(v = 1, 2) \rightarrow B^2\Sigma^+(v = 0, 1)$ LIF excitation spectrum obtained by vertical integration of the indicated horizontal slice anti-Stokes shifted by one vibrational quanta from the laser (i.e., monitoring the $B^2\Sigma^+(v = 0) \rightarrow X^2\Sigma^+(v = 0)$ and $B^2\Sigma^+(v = 1) \rightarrow X^2\Sigma^+(v = 1)$ emission). At the bottom is the medium resolution $X^2\Sigma^+(v = 1, 2) \rightarrow B^2\Sigma^+(v = 0, 1)$ LIF excitation spectrum obtained by vertical integration of the horizontal section anti-Stokes shifted by two vibrational quanta from the laser (i.e., monitoring the $B^2\Sigma^+(v = 1) \rightarrow X^2\Sigma^+(v = 0)$ emission). The Stokes shifted $B^2\Sigma^+(v = 0) \rightarrow X^2\Sigma^+(v = 2)$ emission is also evident in the upper right-hand corner of the 2D spectrum. On the right and left sides are the DLIF spectra obtained by horizontal integration of the indicated vertical rectangular slices centered at the $B^2\Sigma^+-X^2\Sigma^+$ (0, 1) ($\nu = 19{,}684\ cm^{-1}$) and $B^2\Sigma^+-X^2\Sigma^+$ (1, 2) ($\nu = 19{,}592\ cm^{-1}$) bandheads, respectively.

indicated horizontal slice blueshifted (anti-Stokes) by one vibrational quanta from the laser (i.e., monitoring the $B^2\Sigma^+(v = 0) \rightarrow X^2\Sigma^+(v = 0)$ and $B^2\Sigma^+(v = 1) \rightarrow X^2\Sigma^+(v = 1)$ emission) is at the top of Figure 2. At the bottom is the medium resolution $X^2\Sigma^+(v = 1,\ 2) \rightarrow B^2\Sigma^+(v = 0,\ 1)$ LIF excitation spectrum obtained by vertical integration of the horizontal section blueshifted by two vibrational quanta from the laser (i.e., monitoring the $B^2\Sigma^+(v = 1) \rightarrow X^2\Sigma^+(v = 0)$ emission). The redshifted (Stokes) $B^2\Sigma^+(v = 0) \rightarrow X^2\Sigma^+(v = 2)$ emission is also evident in the upper right-hand corner of the 2D spectrum. On the right and left sides of Figure 2 are the medium resolution DLIF spectra obtained by horizontal integration of the indicated vertical rectangular slices centered at the $B^2\Sigma^+-X^2\Sigma^+$ (0, 1) $\tilde{\nu} = 19{,}684\ cm^{-1}$) and $B^2\Sigma^+-X^2\Sigma^+$ (1, 2) ($\tilde{\nu} = 19{,}592\ cm^{-1}$) bandheads, respectively.

The high resolution ($\Delta\lambda = 0.65$ nm full width at half maximum (FWHM)) DLIF spectra in the 440–560 nm range resulting from excitation of the R_1-bandheads of the $B^2\Sigma^+-X^2\Sigma^+$ (0, 1) ($\nu = 19{,}682.3\ cm^{-1}$), $B^2\Sigma^+-X^2\Sigma^+$ (1, 2) ($\nu = 19{,}594.4\ cm^{-1}$), $B^2\Sigma^+-X^2\Sigma^+$ (2, 3) ($\nu = 19{,}513.2\ cm^{-1}$), and $B^2\Sigma^+-X^2\Sigma^+$ (3, 4) ($\nu = 19{,}438.8\ cm^{-1}$) transitions, which are used for lifetime and branching ratio measurements, are presented in Figure 3. The $\Delta v = -1$ bands of the $B^2\Sigma^+-X^2\Sigma^+$ electronic transitions were selected for these measurements because they are less overlapped than the more intense $\Delta v = 0$ bands (Saksena et al. 2008). The spectra of Figure 3 have not been corrected for the wavelength dependence of the spectrometer sensitivity, but have had spectra recorded with the excitation laser blocked and with the ablation laser blocked subtracted. The branching ratios obtained using the integrated peak areas of sensitivity variation corrected spectra are

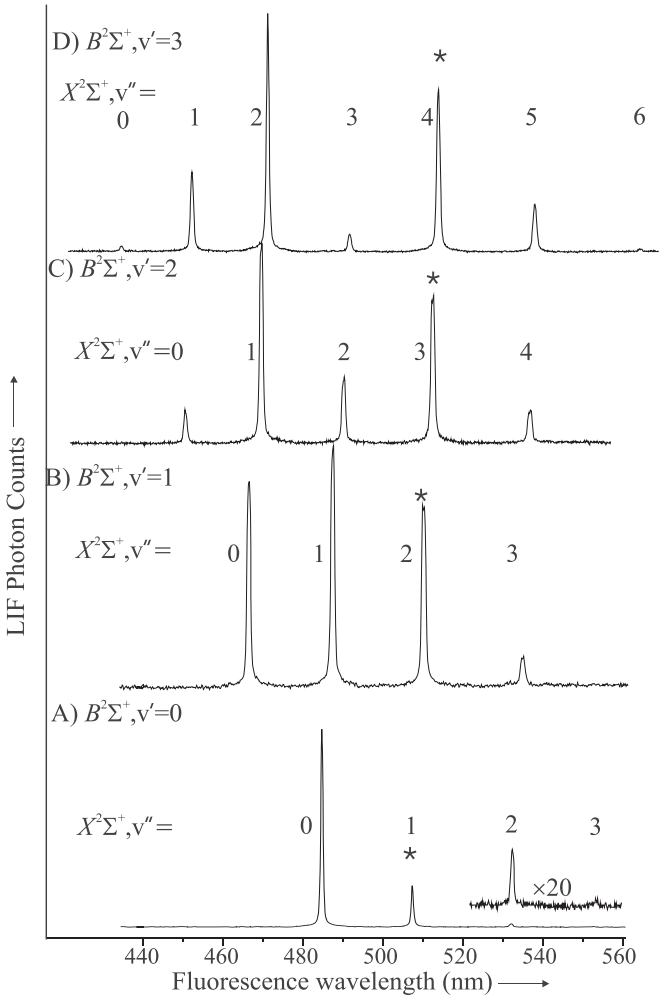

Figure 3. Top: the high-resolution DLIF spectrum resulting from excitation R_1-bandheads of the $B^2\Sigma^+-X^2\Sigma^+$ (0, 1), (1, 2), (2, 3), and (3, 4) bands of AlO.

Table 1
The Branching Ratios (%) of the Dispersed Fluorescence Spectra Resulting from Laser Excitation Near R_1-bandheads of the $B^2\Sigma^+-X^2\Sigma^+$ (0, 1) (1, 2) (2, 3) (3, 4) Transitions of AlO

	$X^2\Sigma^+$						
$v'' =$	0	1	2	3	4	5	6
$B^2\Sigma^+(v = 0)$	79.5[a]	19.0	1.5	…	…	…	…
$B^2\Sigma^+(v = 1)$	28.2	36.0	30.4	5.4	…	…	…
$B^2\Sigma^+(v = 2)$	5.3	40.3	12.9	33.8	7.6	…	…
$B^2\Sigma^+(v = 3)$	0.8	14.4	39.4	3.0	32.3	9.7	0.4

Note.
[a] Estimated errors are ± 0.1%.

presented in Table 1. These values have been obtained assuming that $B^2\Sigma^+(v = 0 - 3) \rightarrow A^2\Pi$ emission contributions are insignificant. The fluorescent decay curves resulting from excitation of the R_1-bandheads of the $B^2\Sigma^+-X^2\Sigma^+$ (0, 1) ($\nu = 19{,}682.3\ cm^{-1}$), $B^2\Sigma^+-X^2\Sigma^+$ (1, 2) ($\nu = 19{,}594.4\ cm^{-1}$), $B^2\Sigma^+-X^2\Sigma^+$ (2, 3)($\nu = 19{,}513.2\ cm^{-1}$), and $B^2\Sigma^+-X^2\Sigma^+$ (3, 4) ($\nu = 19{,}438.8\ cm^{-1}$) transitions are presented in Figure 4. Also presented are the predicted decay curves obtained using least squares optimized lifetimes.

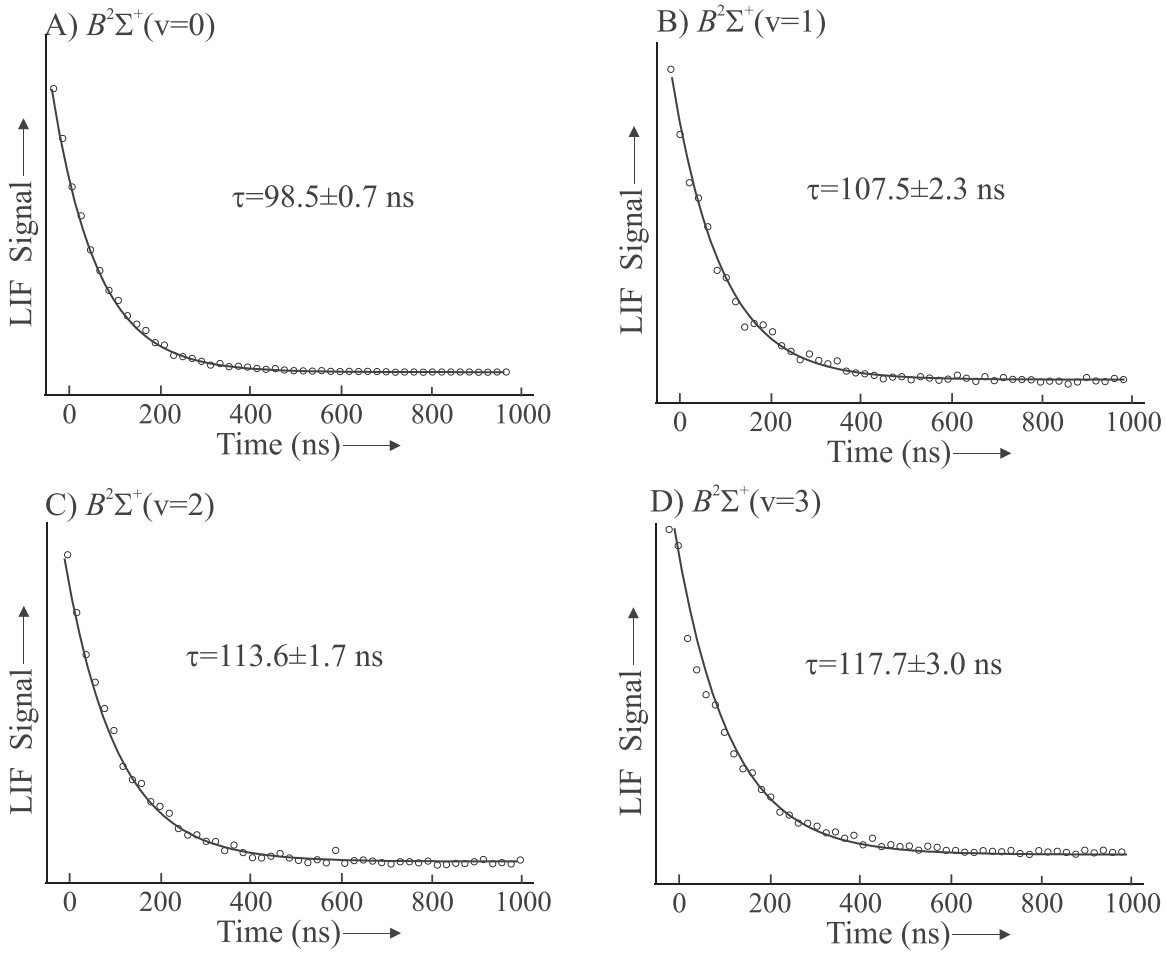

Figure 4. Fluorescent decay curves for the $B^2\Sigma^+$ ($v = 0$–3) states of AlO. The solid lines are predicted decays using the optimized lifetimes.

A prerequisite for the analysis of the optical Stark and Zeeman effect is a precise determination of the relative energies of the field-free, low-rotational levels of the $B^2\Sigma^+(v = 0)$ and $X^2\Sigma^+(v = 1)$ states. Accordingly, the $B^2\Sigma^+$–$X^2\Sigma^+$ (0, 1) band of a skimmed molecular beam sample was recorded and analyzed. The observed and predicted field-free spectra for the $P(3)$, $P(2)$, and $P(1)$ lines of the $B^2\Sigma^+$–$X^2\Sigma^+$ (0, 1) band are presented in Figure 5, while those for the $R(2)$, $R(1)$, and $R(0)$ lines are presented in Figure 6. The fine structure evident in these molecular beam spectra was not resolved in the previous measurements (Saksena et al. 2008), which were recorded at a resolution of 0.05 cm^{-1}. The predicted "stick" spectra, and spectra with coadded Lorentzian lineshapes, obtained using the optimized parameters (see below) are also presented in Figures 5 and 6. A Lorentzian lineshape with FWHM linewidth of 35 MHz, which is somewhat smaller than the observed linewidth of approximately 50 MHz (FWHM), was used to expose the underlying structure of blended lines.

The field-free spectra are complex due to the interactions caused by the nonzero electronic spin and $^{27}Al(I = 5/2)$ nuclear spin angular momenta. The energy level patterns of the low-rotational levels for both the $B^2\Sigma^+(v = 0)$ and $X^2\Sigma^+(v = 1)$ vibronic states are those of a molecule near the Hund's case ($b_{\beta S}$) vector coupling scheme limit because in both state the $^{27}Al(I = 5/2)$ hyperfine interactions are significantly larger than the electron spin–rotation interaction. The hyperfine splitting is primarily due to the Fermi-contact interaction (i.e., the b_F term). In the Hund's case ($b_{\beta S}$) limit the electron spin angular momentum, $\boldsymbol{S}(=1/2)$, is strongly coupled to the ^{27}Al nuclear spin angular momentum, $\boldsymbol{I}(=5/2)$, to give the approximately good intermediate quantum numbers G of 2 and 3. The spectral features at the low wavenumber side of Figures 5 and 6 are the $G'' = 2 \rightarrow G' = 2$ transitions, while those at the high wavenumber side are the $G'' = 3 \rightarrow G' = 3$ transitions. The $G = 2$ and 3 groups of each rotational level in the $B^2\Sigma^+(v = 0)$ and $X^2\Sigma^+(v = 1)$ vibronic states are separated by approximately 5.5 GHz and 2.1 GHz ($\sim 3 \times b_F$), respectively. The angular momentum $\boldsymbol{G}$ is coupled to the rotational angular momentum, $\boldsymbol{N}$, to give the total angular momentum $\boldsymbol{F}$. The corresponding wavefunction, $|(SI_l)G(GN)F>$, is useful for describing the low-rotational energy levels of both states. There are up to 5 and 7 levels ($=(2G+1)$) in the $G = 2$ and 3 groups, respectively. The energy ordering of the 5 or 7 levels, which are characterized by the total angular momentum quantum number F, for a given rotational level of the $X^2\Sigma^+(v = 1)$ state is somewhat irregular (i.e., nonmonotonic) because of the nonnegligible dipolar magnetic and nuclear electric quadrupole coupling hyperfine interactions. Specifically, the energy ordering of F-levels for the $X^2\Sigma^+(N = 1, G = 2, v = 1)$ set is 2, 3, 1 and that for the $X^2\Sigma^+(N = 1, G = 3, v = 1)$ set is 2, 4, 3 (see below). The energy level pattern changes significantly upon rotational excitation because with increasing rotation the ^{27}Al nuclear spin angular momentum $\boldsymbol{I}$ $(=5/2)$ decouples from $\boldsymbol{S}(=1/2)$ and recouples to $\boldsymbol{N}$, and the

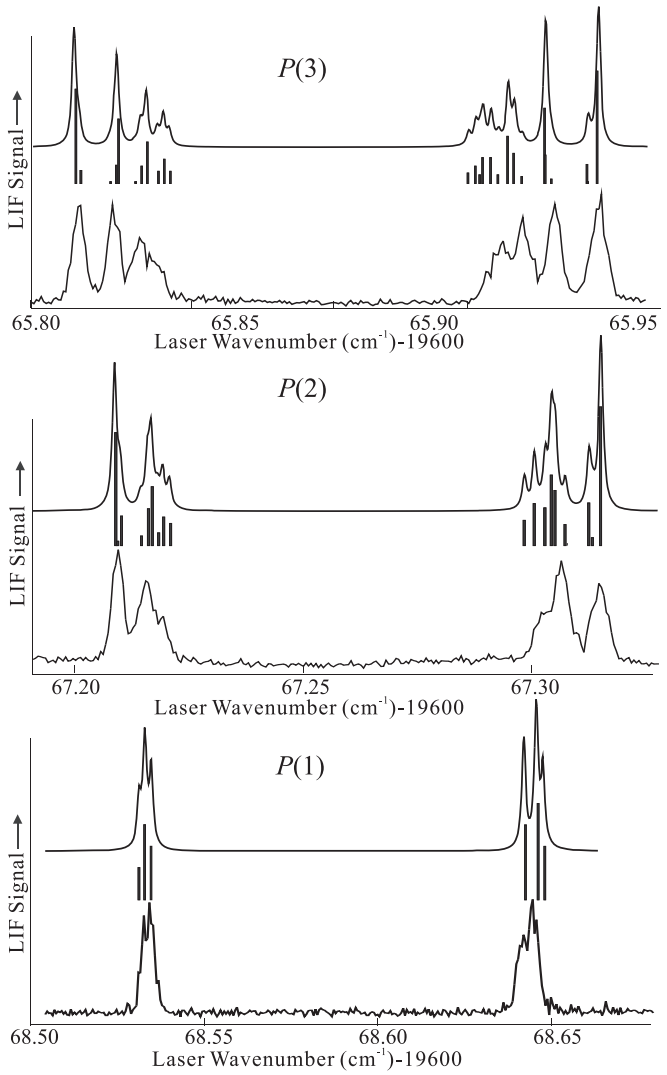

Figure 5. Predicted and observed lowest-J P-branch features of the $B^2\Sigma^+$–$X^2\Sigma^+$ (0, 1) band recorded by laser-induced fluorescence. The group of features on the low wavenumber side are the $G'' = 2 \rightarrow G' = 2$ transitions, while those at the high wavenumber side are the $G'' = 3 \rightarrow G' = 3$ transitions.

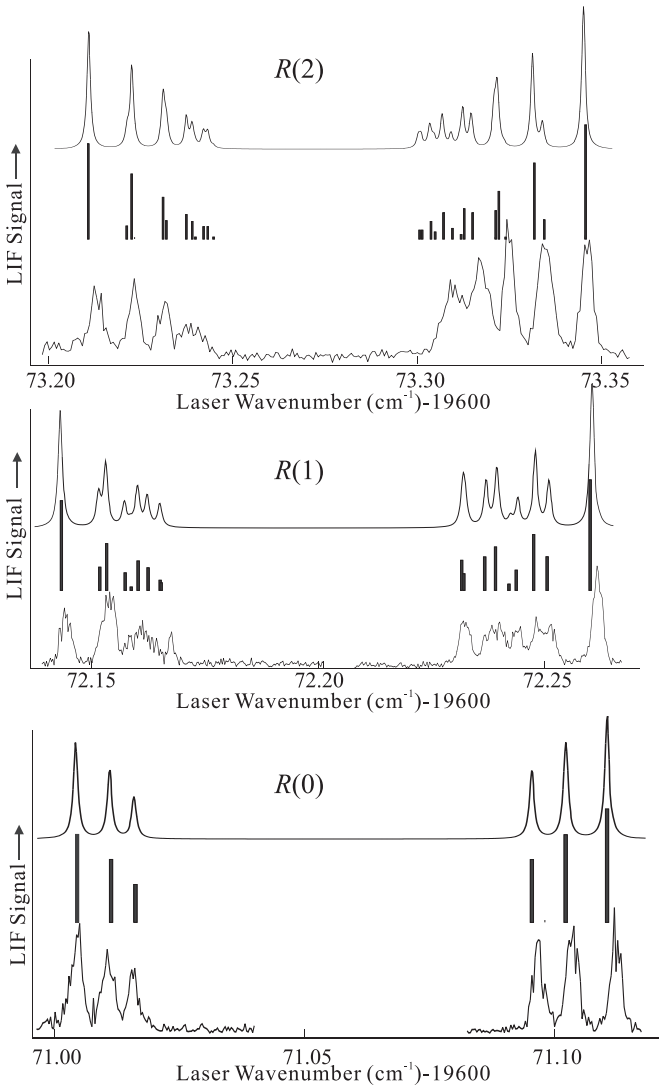

Figure 6. Predicted and observed lowest-J R-branch features of the $B^2\Sigma^+$–$X^2\Sigma^+$ (0, 1) band recorded by laser-induced fluorescence. The group of features on the low wavenumber side are the $G'' = 2 \rightarrow G' = 2$ transitions, while those at the high wavenumber side are the $G'' = 3 \rightarrow G' = 3$ transitions.

energy level pattern becomes that of a molecule near the Hund's case ($b_{\beta J}$) vector coupling scheme limit. The splitting between 38 features associated with the R(0–2) and P(1–3) lines of the $B^2\Sigma^+$–$X^2\Sigma^+$ (0, 1) band (see Figures 5 and 6) were precisely measured and are presented in Table 2, along with the quantum number assignments. Also presented are the differences between the observed splitting and those calculated using the optimized parameters (see below).

The R(0) ($\upsilon = 19{,}671.1\ \mathrm{cm}^{-1}$) and P(1) ($\upsilon = 19{,}668.6\ \mathrm{cm}^{-1}$) lines of the $B^2\Sigma^+$–$X^2\Sigma^+$ (0, 1) band were selected for Stark measurements because these features are relatively unblended and associated with low-J energy levels. The observed and predicted field-free and Stark spectra for the R(0) line with parallel polarization ($\Delta\ M_F = 0$) and a field strength of 4065 $\mathrm{V\,cm}^{-1}$ are given in Figure 7. Also presented are the assignment and a plot of the $X^2\Sigma^+(v = 1,\ N = 0)$ and $B^2\Sigma^+(v = 0,\ N = 1)$ energy levels as a function of applied external electric field strength. The shift of the R(0) line to higher wavenumber (see Figure 7) is primarily due to the second-order Stark shift of the $N = 0$, $G = 2$, and $G = 3$, "+ parity" levels of the $X^2\Sigma^+(v = 1)$ state caused by interaction with the $N = 1$, $G = 2$, and $G = 3$ "−parity" levels, which is higher in energy by approximately $1.26\ \mathrm{cm}^{-1}$. The $N = 1$, $G = 2$, and $G = 3$ levels of the $B^2\Sigma^+(v = 0)$ state are relatively insensitive to the electric field because the second-order Stark shift caused by interaction with the $N = 0$ level is partially negated by that from the $N = 0$ level, and as it turns out, this state has a relatively small molecular frame electric dipole moment, μ_{el}. The observed and predicted field-free and Stark spectra for the P(1) line with parallel polarization ($\Delta\ M_F = 0$) and a field strength of 4065 $\mathrm{V\,cm}^{-1}$ are given in Figure 8. The spacing of the $F = 1$, 2, and 3 levels of the $G = 2$ group and the $F = 2$, 3, and 4 of the $G = 3$ group in the $X^2\Sigma^+(v = 1,\ N = 1)$ state are very small because of the small spin–rotation interaction. As a result, upon application of the electric field M_N becomes the approximately good quantum number and the $G = 2$ and $G = 3$ levels regroup into two widely spaced sets that are characterized by $M_N = 0$ and ± 1. The approximately good selection rule for the parallel polarization becomes $\Delta M_N = 0$. Spectral features of the P(1) line shift to a lower wavenumber due to the combined second-order Stark shift of

Table 2
Fine Structure Splittings of the Low-rotational Lines of the $B^2\Sigma^+$–$X^2\Sigma^+$ (0, 1) Transition of AlO

Line	Lower	Upper	Obs.	Dif.[a]
	G'', F'' → G', F'	G'', F'' → G', F'	(MHz)	(MHz)
$R(0)$	2, 2 → 2, 3	3, 3 → 3, 4	3841	−29
	2, 2 → 2, 3	2, 2 → 2, 2	199	−15
	2, 2 → 2, 2	2, 2 → 2, 1	166	13
	3, 3 → 3, 2	3, 3 → 3, 3	203	−11
	3, 3 → 3, 3	3, 3 → 3, 4	271	8
$R(1)$	2, 3 → 2, 4	3, 4 → 3, 5	4308	−40
	2, 3 → 2, 4	2, 2 → 2, 3	314	−7
	3, 2 → 3, 1	3, 4 → 3, 4	933	19
$R(2)$	2, 4 → 2, 5	3, 5 → 3, 6	4686	36
	2, 4 → 2, 5	2, 3 → 2, 4	378	13
	2, 3 → 2, 4	2, 2 → 2, 3	289	27
	3, 2 → 3, 2	3, 3 → 3, 4	249	32
	3, 3 → 3, 4	3, 4 → 3, 5	318	19
	3, 4 → 3, 5	3, 5 → 3, 6	404	−28
$P(1)$	2, 3 → 2, 2	3, 4 → 3, 3	3502	9
	3, 3 → 3, 3	3, 4 → 3, 3	101	5
$P(2)$	2, 4 → 2, 3	3, 5 → 3, 4	3864	−33
	2, 4 → 2, 3	2, 3 → 2, 2	236	−18
	3, 4 → 3, 3	3, 5 → 3, 4	319	−26
$P(3)$	2, 5 → 2, 4	3, 6 → 3, 5	4260	−7
	2, 5 → 2, 4	2, 4 → 2, 3	300	−8
	2, 4 → 2, 3	2, 3 → 2, 2	210	3
	3, 3 → 3, 2	3, 4 → 3, 3	172	−7
	3, 4 → 3, 3	3, 5 → 3, 4	265	−3
	3, 5 → 3, 4	3, 6 → 3, 5	375	−7
Std. Dev. = 21 MHz				

Note.
[a] The difference between the observed and the calculated splitting obtained using the optimized spectroscopic parameters given in Table 4.

the $N = 0$, $G = 2$, and $G = 3$, "+ parity" levels of the $B^2\Sigma^+(v = 0)$ state to lower energy (∼145 MHz at 4065 V cm^{-1}) and a shift to higher energy (∼450 MHz at 4065 V cm^{-1}) of the $M_N = 0$ levels of the $X^2\Sigma^+$ ($v = 1$, $N = 1$) state. The 26 measured Stark shifts, assignments, and differences between the observed and calculated shifts are given in Table 3.

The observed field-free and Zeeman spectra for the $P(1)$ ($\upsilon = 19{,}668.6\,\mathrm{cm}^{-1}$) lines of the $B^2\Sigma^+$–$X^2\Sigma^+$ (0, 1) transition are presented on the left-hand side of Figure 9. The observed spectrum was recorded with perpendicular polarization ($\Delta M_F = \pm 1$) and a magnetic field of 1454 G. Also presented in Figure 9 are predicted perpendicular polarization Zeeman spectra in the 0–1500 G range in 300 G steps. On the right-hand side of Figure 9 are magnetic tuning curves of the associated energy levels. The energy level plot and predicted spectra used the optimized set of field-free parameters and the expected magnetic g-factors (i.e., no optimization). The energy level plot illustrates that upon application of the magnetic field both the electronic spin, $\boldsymbol{S}$, and nuclear spin, $\boldsymbol{I}$, rapidly decouple from the molecular frame and become quantized in the laboratory axis defined by the magnetic field. Specifically, upon application of the magnetic field the 36 M_F levels associated with the $X^2\Sigma^+(v = 1, N = 1)$ state separate into two widely spaced groups of 18 levels characterized by the projection of the electronic spin angular momentum $M_S(= \pm 1/2)$. Each of these two groups consists of six sets characterized by projection of the nuclear spin angular momentum $M_I(= \pm 5/2, \pm 3/2$, and $\pm 1/2)$. Each of those six groups consists of three levels characterized by projection of the rotational angular momentum $M_N(= \pm 1$ and 0). Similarly, the 12 M_F levels associated the $B^2\Sigma^+(v = 0, N = 0)$ state separate into two groups containing six levels each associated with $M_S(= \pm 1/2)$. The decoupling of $\boldsymbol{S}$ and $\boldsymbol{I}$ from the molecular frame occurs at a higher magnetic field for the $B^2\Sigma^+(v = 0, N = 0)$ state than the $X^2\Sigma^+(v = 1, N = 1)$ state because both the magnetic hyperfine interaction and the spin–rotation interaction are larger.

4. Analysis

The effective Hamiltonian for the $X^2\Sigma^+(v = 1)$ and $B^2\Sigma^+(v = 0)$ states included rotation (B and D), spin–rotation (γ), magnetic hyperfine (b_F and c), nuclear electric quadrupole (e^2Qq_0) terms, and the origin (T_v) (Brown & Carrington 2003):

$$\hat{\boldsymbol{H}}^{\mathrm{eff}}(^2\Sigma^+) = T\mathrm{v} + B\hat{\boldsymbol{N}}^2 - D(\hat{\boldsymbol{N}}^2)^2 + \gamma\hat{\boldsymbol{N}}\cdot\hat{\boldsymbol{S}} + b_F\hat{\boldsymbol{I}}\cdot\hat{\boldsymbol{S}} + \frac{c}{3}(3\hat{I}_z\hat{S}_z - \hat{\boldsymbol{I}}\cdot\hat{\boldsymbol{S}}) + e^2Qq_0\frac{(3\hat{I}_z^2 - \hat{\boldsymbol{I}}^2)}{4I(2I-1)}. \quad (3)$$

The field-free eigenvalues and eigenvectors were obtained by diagonalizing a 12 × 12 matrix representation of $\hat{\boldsymbol{H}}^{\mathrm{eff}}(^2\Sigma^+)$ constructed in a Hund's case ($a_{\beta J}$) basis set. A Hund's case ($a_{\beta J}$) basis set is used for convenience even though the energy level pattern is that of a molecule near the Hund's case ($b_{\beta S}$) limit. Spectra predicted using the previously determined parameters from the combined analysis (Launila & Berg 2011) exhibited slight difference in the hyperfine splitting as compared to the observed spectra given in Figures 5 and 6. The previous analysis provided only an estimate of the b_F parameter for the $B^2\Sigma^+(v = 0)$, which was derived from line broadening. The observed splittings of Table 2 were least squares fit to optimize $b_F(B^2\Sigma^+(v = 0))$ while constraining all other parameters to the previously determined values (Launila & Berg 2011). (Note that that "b_F," and not "b" as indicated, is listed in Table 3 of Launila & Berg 2011). The newly determined value of 0.0627 ± 0.0002 cm^{-1} is consistent with the estimate (Launila & Berg 2011) of 0.057 cm^{-1}. The standard deviation of the fit is 22 MHz, which is consistent with estimated measurement uncertainty. The complete set of parameters used to model the spectra is given in Table 4.

The interaction with the static electric field was modeled using the standard Stark Hamiltonian operator,

$$\hat{\boldsymbol{H}}^{\mathrm{Stark}} = -\boldsymbol{\mu}_{el}\cdot\boldsymbol{E}, \quad (4)$$

where $\hat{\boldsymbol{E}}$ is the external electric field and $\hat{\boldsymbol{\mu}}_{el}$ is the electric dipole moment operator. The data are only sensitive to the magnitude of the electric dipole moment, $|\mu_{el}|$. The matrix representation of $\hat{\boldsymbol{H}}^{\mathrm{Stark}}$ is diagonal in the projection of the total angular momentum quantum number, M_F, but has infinite dimension. The matrix was truncated to include only $F = 0$–6 and the eigenvalues and eigenvectors were obtained by diagonalizing the resulting 84 × 84 matrix constructed in a

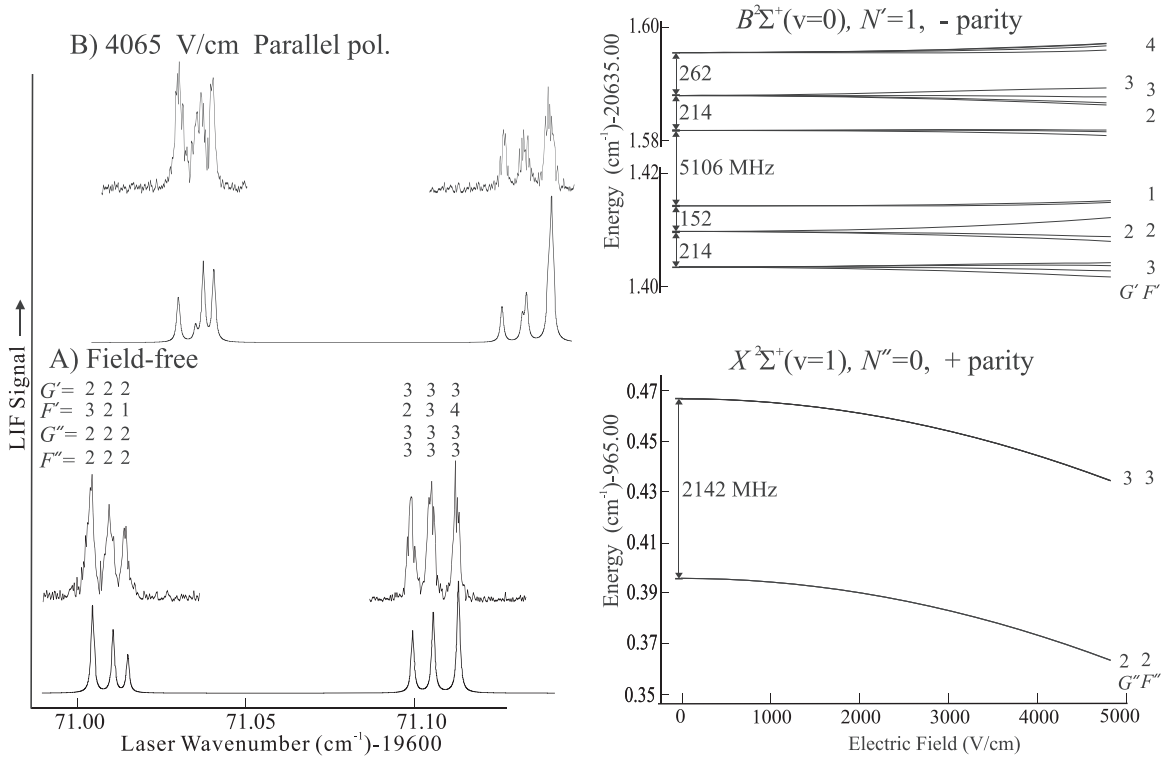

Figure 7. Left: the field-free and Stark spectra for the $R(0)$ branch features of the $B^2\Sigma^+ - X^2\Sigma^+$ (0, 1) band recorded in the presence of a 4065 V cm^{-1} field with parallel ($\Delta M_F = 0$) orientation of the static electric field relative to that of the linearly polarized laser. Right: the tuning of the energy levels associated with the $R(0)$ line. The ^{27}Al($I = 5/2$) hyperfine interaction in both states is larger than the spin–rotation interaction causing the energy levels to be that of a near Hund's case ($b_{\beta S}$) molecule where $\boldsymbol{G}(\equiv \boldsymbol{I} + \boldsymbol{S})$ is the appropriate intermediate angular momentum.

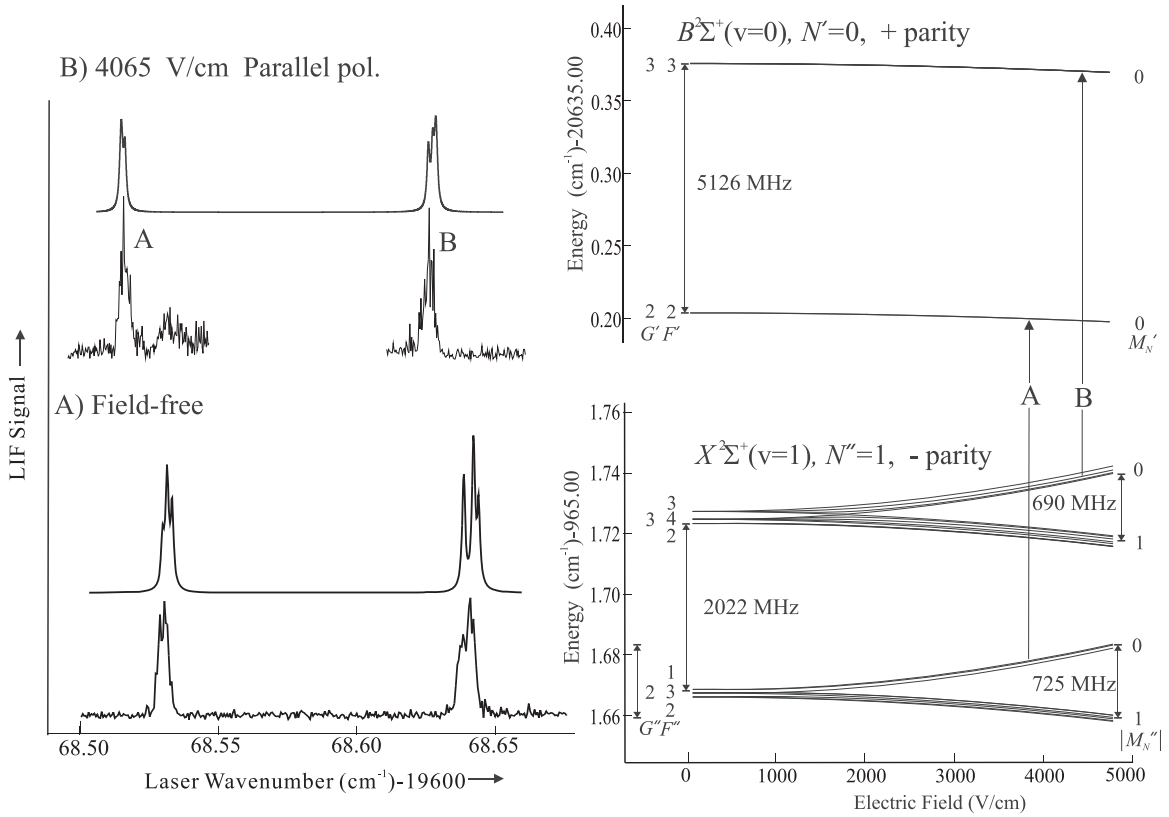

Figure 8. Left: the field free and Stark spectra for the $P(1)$ branch feature of the $B^2\Sigma^+ - X^2\Sigma^+$ (0, 1) band recorded in the presence of a 4065 V cm^{-1} field with parallel ($\Delta M_F = 0$) orientation. Right: the tuning of the energy levels associated with the $P(1)$ line. Upon application of the electric field M_N becomes the approximately good quantum number and the $G = 2$ and $G = 3$ levels regroup into two widely spaced sets that are characterized by $M_N = 0$ and ± 1.

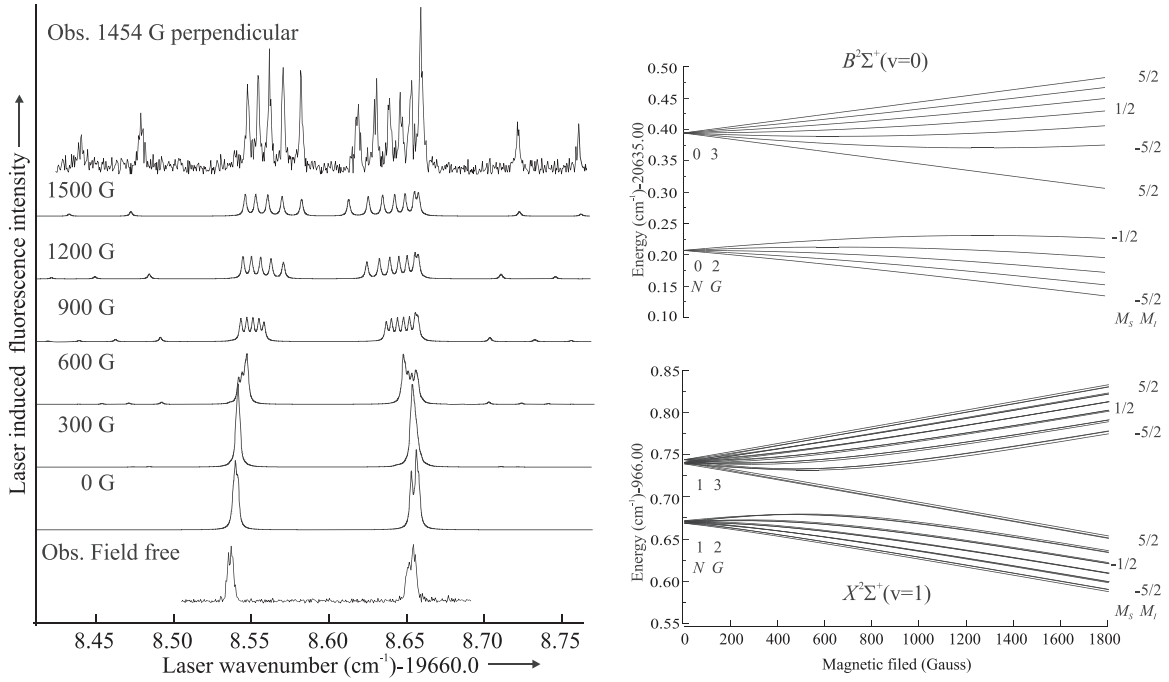

Figure 9. Left: the observed and predicted Zeeman spectra for the $P(1)$ ($\upsilon = 19{,}668.6$ cm^{-1}) lines of the $B^2\Sigma^+$–$X^2\Sigma^+$ (0, 1) transition recorded with perpendicular polarization ($\Delta M_F = \pm 1$) and a magnetic field of 1454 G. Right: the magnetic tuning of the energy levels associated with the $P(1)$ lines. The energy level plot and predicted spectra used the optimized set of field-free parameters and the expected magnetic g-factors (i.e., no optimization). Upon application of the magnetic field both the electronic spin, $\boldsymbol{S}$, and nuclear spin, $\boldsymbol{I}$, rapidly decouple from the molecular frame and become quantized in the laboratory axis and $M_S(= \pm 1/2)$ and $M_I(= \pm 5/2, \pm 3/2$ and $\pm 1/2)$ become the approximately good quantum numbers.

Table 3
Observed and Calculated Stark Shift of the $R(0)$ and $P(1)$ Lines of the $B^2\Sigma^+$–$X^2\Sigma^+$ (0, 1) Transition of AlO

Lines	*Pol.*	F'', $\lvert M_F''\rvert$	F', $\lvert M_F'\rvert$	Field (V cm^{-1})	Shift (MHz)	Obs. − Calc. (MHz)
$R(0)$, $G = 2$	⊥	2, 2	3, 3	4065	686	9
		2, 2	2, 1		709	11
		2, 2	1, 1		751	21
$R(0)$, $G = 3$	⊥	3, 3	2, 2		700	3
		3, 0	3, 1		694	6
		3, 1	4,2		716	−29
$R(0)$, $G = 2$	∥	2, 1	3, 1		733	2
		2, 2	2, 2		758	−19
		2, 0	1, 0		750	11
$R(0)$, $G = 3$	∥	3, 0	2, 0		735	10
		3, 3	3, 3		758	1
		3, 0	4,0		763	3
$P(1)$, $G = 2$	⊥	2, 3	2, 2		89	16
$P(1)$, $G = 3$		4, 4	3, 3		50	−23
$P(1)$, $G = 2$	∥	3, 2	2, 2		−574	−33
$P(1)$, $G = 3$		2, 2	2, 2		−578	26
$R(0)$, $G = 2$	∥	2, 1	3, 1	3070	405	−18
		2, 2	2, 2		411	−32
		2, 0	1, 0		395	−26
$R(0)$, $G = 3$	∥	3, 0	2, 0		435	17
		3, 3	3, 3		417	−21
		3, 0	4,0		441	7
$P(1)$, $G = 2$	⊥	2, 3	2, 2		37	−5
$P(1)$, $G = 3$		4, 4	3, 3		50	8
$P(1)$, $G = 2$	∥	3, 2	2, 2		−321	−33
$P(1)$, $G = 3$		2, 2	2, 2		−356	5

Std. fit: 19 MHz

Hund's case ($a_{\beta J}$) basis. The Stark induced shifts of Table 3 were least squares fit to determine optimized values of $|\mu_{el}|$ of 1.94(8) D and 4.45(3) D for the $B^2\Sigma^+(v = 0)$ and $X^2\Sigma^+(v = 1)$ states, respectively. The standard deviation of the fit is 19 MHz, consistent with estimated measurement uncertainty, and the correlation coefficient is −0.19.

Table 4
Spectroscopic Parameters for the $B^2\Sigma^+(v=0)$ and $X^2\Sigma^+(v=1)$ States of AlO

Parameter[a]	$X^2\Sigma^+(v=1)$[b]	$B^2\Sigma^+(v=0)$[c]
B	0.6232688516	0.6018559
D	1.1134×10^{-6}	1.625×10^{-6}
γ	0.532035×10^{-3}	0.014
γ_D	$-1.7111838 \times 10^{-7}$	-1.0×10^{-7}
b_F	0.0238	0.0627(2)[c]
c	0.005524	...
eQq_0	-7.24×10^{-4}	...
T_v	965.45060	20635.3115
g_S	2.002	2.002
g_l	-4.2×10^{-4}	−0.0116
$\lvert\mu_{el}\rvert$	1.94(8) D	4.45(3) D

Notes.
[a] Units: B, D, ... T_v in wavenumbers, cm^{-1}; electric dipole moment in Debye, D.
[b] T_v, B, D, γ, and γ_D, from Launila & Berg (2011); b_F, c and eQq_0 from Goto et al. (1994).
[c] T_v, B, D, γ, and γ_D, from Launila & Berg (2011); b_F from present study. The numbers in parentheses represent a 90% confidence limit.

Table 5
The Permanent Electric Dipole Moments, μ_{el} (Debye)

	Exp.[a]	Predicted				
		A[b]	B[c]	C[d]	D[e]	E[f]
$X^2\Sigma^+$	4.45(3)($v=1$)	5.08($v=0$) 4.96($v=1$)	4.24(μ_e)	4.26(μ_e)	4.60(μ_e) (4.36)	4.39[g]
$B^2\Sigma^+$	1.94(8)($v=0$)	1.88($v=0$)	1.27(μ_e)	1.21(μ_e)		2.10[g] (1.81)

Notes.
[a] Obtained from the analysis of the optical Stark spectrum of the $R(0)$ and $P(1)$ lines of the $B^2\Sigma^+$–$X^2\Sigma^+$ (0, 1) band.
[b] Yoshimine et al. (1973).
[c] Zenouda et al. (1999).
[d] Honjou (2010).
[e] Lengsfield & Liu (1982).
[f] Patrascu et al. (2015).
[g] Evaluated at 1.76 Å. The numbers in parentheses are values at R_e obtained from dipole moment curves.

The Zeeman effect was modeled using an effective Hamiltonian having terms accounting for interaction with the magnetic moments associated with the electronic spin angular momentum (Brown & Carrington 2003):

$$\hat{H}^{\mathrm{Zee}} = \hat{\mu}_m \cdot \hat{B} \approx g_S \mu_B \hat{S}_Z B_z + g_l[\hat{S}_x B_x + \hat{S}_y B_y]. \quad (5)$$

The g_l term describes the anisotropic contribution to the electron spin Zeeman effect. The small magnetic moments associated with rotation and nuclear spin were neglected. In the effective Hamiltonian approach, the electronic spin g-factor, g_S, is considered a variable and may vary significantly from the 2.002 value of a free electron. The g_l parameter is theoretically related to the spin–rotation parameter, γ, by the Curl relationship (Brown & Carrington 2003) $\left(g_l = -\frac{\gamma}{2B}\right)$, which for the $X^2\Sigma^+(v=1)$ and $B^2\Sigma^+(v=0)$ states give -4.2×10^{-4} and -0.0116, respectively. As it turns out the Zeeman effect could be accurately predicted (see Figure 9) by assuming $g_S = 2.002$ and the Curl relationship values for g_l.

Modeling the field-free, Stark, and Zeeman spectra was performed by generating either a 12×12 or 84×84 electric dipole TDM matrix, $\underline{\underline{\mu}}$, in the Hund's case ($a_{\beta J}$) basis. The matrices were cross multiplied with the upper and lower state eigenvectors, $\underline{a}(B^2\Sigma^+, X^2\Sigma^+)$, to obtain the appropriate TDM, TDM:

$$\mathrm{TDM}(B^2\Sigma^+ \leftrightarrow X^2\Sigma^+) = \underline{a}^{\mathrm{T}}(B^2\Sigma^+) \cdot \underline{\underline{\mu}} \cdot \underline{a}(X^2\Sigma^+). \quad (6)$$

The TDM was then squared and multiplied by the Boltzmann factors appropriate for the approximate 30 K internal temperature of the supersonic expansion. A Lorentzian line shape with a FWHM of 35 MHz was superimposed to give the predicted spectra as shown in Figures 5–9.

5. Discussion

The previously determined spectroscopic parameters (Toerring & Herrmann 1989; Yamada et al. 1990; Goto et al. 1994; Launila & Berg 2011; Breier et al. 2018) augmented by the newly determined value for $b_F(B^2\Sigma^+(v=0))$, accurately

Table 6
Calculated Einstein A-coefficient, $A_{v'J',v''J''}$ (Patrascu et al. 2015), and Hönl–London Factors, $S_{J',J''}$, for the R_1 Bandheads of the $B^2\Sigma^+ \rightarrow X^2\Sigma^+$ Transitions of AlO

		$X^2\Sigma^+$							
$B^2\Sigma^+$	$v''=$	0	1	2	3	4	5	6	$S_{J',J''}$
$v=0$	$A_{0,20.5,v'',19.5}$	4.07×10^6	1.08×10^6	1.05×10^5	3.73×10^3	1.90×10^1	1.23	1.44	20.4878
$v=1$	$A_{1,21.5,v'',20.5}$	1.59×10^6	1.80×10^6	1.50×10^6	2.40×10^5	1.09×10^4	3.86×10^1	0.175	21.4884
$v=2$	$A_{2,22.5,v'',21.5}$	3.62×10^5	2.06×10^6	6.62×10^5	1.56×10^6	3.66×10^5	1.97×10^4	6.35×10^1	22.4889
$v=3$	$A_{3,23.5,v'',22.5}$	6.11×10^4	7.82×10^5	1.96×10^6	1.65×10^5	1.45×10^6	4.68×10^5	2.85×10^4	23.4893

simulate the field-free high-resolution excitation spectrum of the $B^2\Sigma^+$–$X^2\Sigma^+$ (0, 1) band as illustrated in Figures 5 and 6. Similarly, the magnetic tuning of the low-J branch features of the $B^2\Sigma^+$–$X^2\Sigma^+$ (0, 1) band is accurately modeled by constraining g_S to that of a free electron and g_l to the values given by the Curl relationship. The optical Stark spectrum for the $B^2\Sigma^+$–$X^2\Sigma^+$ (0, 1) band is also readily simulated using the extracted $|\mu_{el}|$ values of 4.45(3) D and 1.94(8) D for the $X^2\Sigma^+(v=1)$ and $B^2\Sigma^+(v=0)$ states, respectively. The experiment only determines $|\boldsymbol{\mu}_{el}|$, but an $Al^{+\delta}O^{-\delta}$ charge distribution in both states is expected. The magnetic hyperfine structure in the $X^2\Sigma^+$ state was used to predict (Yamada et al. 1990) that the $Al^{+2}O^{-2}$, $Al^{+1}O^{-1}$, and Al^0O^0 charge distributions contribute 19.1, 13.1, and 67.8% to the $X^2\Sigma^+$ state. Near the equilibrium bond distance, the dominant configurations for the $X^2\Sigma^+$ and $B^2\Sigma^+$ state are $..6\sigma^27\sigma2\pi^4$ and $..6\sigma7\sigma^22\pi^4$, respectively, where the 6σ and 7σ are predominately O $2p$ and Al $3s$, respectively. Therefore, excitation to the $B^2\Sigma^+$ state lowers the $Al^{+2}O^{-2}$ and increases the $Al^{+1}O^{-1}$ charge contribution but leaving a $Al^{+\delta}O^{-\delta}$ charge distribution, which is consistent with the most recent ab initio prediction (Patrascu et al. 2015). The determined $|\boldsymbol{\mu}_{el}|$ values are compared with theoretical predictions in Table 5. All calculations (Yoshimine et al. 1973; Lengsfield & Liu 1982; Zenouda et al. 1999; Honjou 2010; Patrascu et al. 2015) predict $|\boldsymbol{\mu}_{el}|$ values for the $X^2\Sigma^+$ state which are in reasonably good agreement with the experimental value for the $X^2\Sigma^+(v=1)$ state. The most recent prediction gives $|\boldsymbol{\mu}_{el}|$ values of 4.39 D and 2.10 D for the $X^2\Sigma^+$ and $B^2\Sigma^+$ states, respectively, for an internuclear separation of 1.76 Å (Patrascu et al. 2015); whereas, the equilibrium bond distances, R_e, for the $X^2\Sigma^+$ and $B^2\Sigma^+$ states are (Patrascu et al. 2014) 1.618 Å and 1.667 Å, respectively. Extrapolation of the dipole moment curves (Patrascu et al. 2015), which in the region of R_e are relatively flat for the $X^2\Sigma^+$ state but exhibits a significant negative slope for the $B^2\Sigma^+$ state, to R_e gives values of approximately 4.38 D and 1.84 D, which are in closer agreement with the experimentally determined values of 4.45(3) D and 1.94(8) D.

A primary objective of the current work is to use the experimentally derived lifetimes and branching ratios to determine the magnitude of the vibronic TDM, $|\mu_{iv',fv''}|$, via Equation (2) and compare those experimental values with $|\mu_{iv',fv''}|$ values extracted from the predicted (Patrascu et al. 2015) Einstein A-coefficient, $A_{v'J',v''J''}$. The experimentally determined radiative lifetimes of 98.5 ± 0.7, 107.5 ± 2.3, 113.6 ± 1.7 for the $B^2\Sigma^+(v=0$–$2)$ are in somewhat better agreement with the 100 ± 7, 102 ± 7, and 102 ± 4 ns values by Dagdigian et al. (1975) as compared to the 128.6 ± 6, 125.5 ± 2.6, and 130.5 ± 7 ns values by Johnson et al. (1972). The newly determined experimental values are somewhat larger than the recently predicted (Patrascu et al. 2015) values of 92.4, 94.5, and 96.7 ns. The measured 117.7 ± 3.0 ns value for $B^2\Sigma^+(v=3)$ continues the trend of increasing with vibrational excitation which is consistent with the recent prediction.

The tabulated (Patrascu et al. 2015) $A_{v'J',v''J''}$ values are related to the line strength factor $S_{v'J',v''J''}$ via Equation (1). The $S_{v'J',v''J''}$ line strength factor is the product of $|\mu_{iv',fv''}|^2$ and the Hönl–London factor $S_{J',J''}$:

$$S_{v'J',v''J''} = S_{J',J''}\,|\mu_{iv',fv''}|^2. \quad (7)$$

The nuclear spin was ignored in the $A_{v'J',v''J''}$ prediction (Patrascu et al. 2015) and consequently the predicted eigenfunctions for the $B^2\Sigma^+$ and $X^2\Sigma^+$ states are those of a pure Hund's case (b). Hence, the required Hönl–London factors needed to convert the tabulated $A_{v'J',v''J''}$ values are those for a Hund's case (b) → Hund's case (b) transition (Watson 2008):

$$S_{J',J''}(\text{case}(b)) = (2J'+1)(2J''+1)\begin{Bmatrix} N' & 1 & N'' \\ J'' & 1/2 & J' \end{Bmatrix}^2 \times (2N'+1)(2N''+1)\begin{pmatrix} N' & 1 & N'' \\ 0 & 0 & 0 \end{pmatrix}^2. \quad (8)$$

The required $S_{J',J''}$ values needed for interpretation of the observed DLIF branching ratios are readily determined using Equation (8) and the J-values associated with R_1-bandheads of the $B^2\Sigma^+$–$X^2\Sigma^+$ (0, 1), $B^2\Sigma^+$–$X^2\Sigma^+$ (1, 2), $B^2\Sigma^+$–$X^2\Sigma^+$ (2, 3), and $B^2\Sigma^+$–$X^2\Sigma^+$ (3, 4) transitions which are (Saksena et al. 2008) 19.5, 20.5, 21.5, and 22.5, respectively. Note that $N = J\text{-}1/2$ for the R_1 branch. The ab initio predicted (Patrascu et al. 2015) $A_{v'J',v''J''}$ values and the $S_{J',J''}$ values from Equation (8) are collected in Table 6. The $A_{v'J',v''J''}$ values and the $S_{J',J''}$ values of Table 6 are combined to give the predicted $\mu_{iv',fv''}$ presented in Table 7. Also presented in Table 7 are the experimentally determined $|\mu_{iv',fv''}|$ values derived from the measured lifetimes and branching ratios (see Table 1) using Equation (2) as well as those derived from the previously published (Hebert et al. 1980) experimental $A_{iv',fv''}$ values. The quantitative agreement between the previously determined experimental values (Hebert et al. 1980) and those from the current study is poor although the general trend is consistent. The agreement between the TDM extracted from the ab initio calculated $A_{v'J',v''J''}$ values (Patrascu et al. 2015) and the newly determined experimental $|\mu_{iv',fv''}|$ values of the current study is very good both in magnitude and trend. A perusal of the differences between the observed and predicted $|\mu_{iv',fv''}|$ values, which are also presented in Table 7, indicate that the ab initio calculated values are typically 0.05 D larger than the experimentally observed values. This is consistent with the fact that the observed lifetimes are slightly larger than the predicted values and suggest that the predicted TDMs are a slight overestimate. The potential energy curves used to predict

Table 7
The Magnitude of the Vibronic Transition Dipole Moments, $|\mu_{iv',fv''}|$, for the $B^2\Sigma^+ \rightarrow X^2\Sigma^+$ Transitions of AlO

		$X^2\Sigma^+$						
	$v''=$	0	1	2	3	4	5	6
$B^2\Sigma^+$ ($v=0$)	Obs.(Previous)[a]	1.474	0.869	0.044	0.061	⋯	⋯	⋯
	Obs.(New)[b]	1.710	0.898	0.270	<0.10	⋯	⋯	⋯
	Calc.[c]	1.739	0.962	0.323	0.066	0.0051	0.0014	0.0016
	Dif.[d]	−0.029	−0.064	−0.053	⋯	⋯	⋯	⋯
$B^2\Sigma^+$ ($v=1$)	Obs.(Previous)	0.954	0.887	0.968	0.656	0.335	⋯	⋯
	Obs.(New)	0.917	1.110	1.094	0.496	⋯	⋯	⋯
	Calc.	1.022	1.164	1.141	0.491	0.113	0.0073	0.0005
	Dif.	−0.105	−0.054	−0.047	0.005	⋯	⋯	⋯
$B^2\Sigma^+$ ($v=2$)	Obs.(Previous)	0.524	0.959	0.497	0.947	0.802	0.148	
	Obs.(New)	0.363	1.077	0.651	1.129	0.582	⋯	⋯
	Calc.	0.459	1.171	0.710	1.170	0.609	0.152	0.0095
	Dif.	−0.096	−0.094	−0.059	−0.041	−0.027	⋯	⋯
$B^2\Sigma^+$ ($v=3$)	Obs.(Previous)	0.259	0.683	0.836	0.241	0.885	0.908	0.584
	Obs.(New)	0.131	0.595	1.052	0.310	1.092	0.642	0.135
	Calc.	0.178	0.680	1.150	0.357	1.134	0.692	0.184
	Dif.	−0.047	−0.085	−0.098	−0.047	−0.042	−0.050	−0.049

Notes.
[a] Obtained using the previously derived $A_{iv',fv''}$ values (Hebert et al. 1980) and Equation (2).
[b] Obtained using the branching ratios given in Table 1 and measured radiative lifetimes, $\tau_{iv'}$.
[c] Obtained using the calculated Einstein A-coefficient, $A_{v'J',v''J''}$, (Patrascu et al. 2015), Hönl–London factors from Equation (8), $S_{J',J''}$ and the experimental transition wavenumbers.
[d] The difference between "Obs.(New)" and "Calc"

the TDMs (Patrascu et al. 2015) should be very accurate because they were refined using experimental data and are not purely ab initio (Patrascu et al. 2014). Alternatively, there could be a source of systematic errors in the determination of the experimental branching ratios performed here due to the assumption that the $B^2\Sigma^+ \rightarrow A^2\Pi$ emission is negligible. Inclusion of $B^2\Sigma^+ \rightarrow A^2\Pi$ emission would reduce the experimental branching ratios given in Table 1; hence, increasing the experimental $|\mu_{iv',fv''}|$ values brings them in closer agreement with the ab initio values. Based upon the predicted $A_{v'J',v''J''}$ values for the $B^2\Sigma^+ \rightarrow A^2\Pi$ transitions (Patrascu et al. 2015), the error associated with omission of the $B^2\Sigma^+ \rightarrow A^2\Pi$ emission is estimated to be less than 2%.

6. Summary

An internally cold sample of AlO has been generated via laser ablation techniques and characterized using medium and high-resolution laser-induced fluorescence spectroscopy. The radiative lifetimes and branching ratios of the $B^2\Sigma^+(v=0$–$3)$ states have been precisely determined using LIF detection of a free-jet expansion sample. The TDMs for numerous bands of the $B^2\Sigma^+$–$X^2\Sigma^+$ electronic transition and the permanent electric dipole moments of the $B^2\Sigma^+(v=0)$ and $X^2\Sigma^+(v=1)$ states have been experimentally determined and compared with theoretically predicted values. The recently predicted (Patrascu et al. 2015) transition dipole moments for the $B^2\Sigma^+ \rightarrow X^2\Sigma^+$ are in very good agreement, but systematically lower by approximately 0.05 D when compared with the experimentally determined values. It has been demonstrated that the Zeeman tuning of the low-rotational features of the $B^2\Sigma^+$–$X^2\Sigma^+$ electronic transition can be accurately modeled using the expected g-factors and newly derived field-free parameters. The determined TDMs and permanent electric dipole moment for the $X^2\Sigma^+$ state will facilitate conversion of spectral intensities to column densities and serve as bench marks for assessment of ab initio and semi-empirical electronic structure predictions.

This work has been supported by the National Science Foundation, Division of Astronomical Sciences (AST-1715049). The authors thank Dr. Anh Le (School of Molecular Sciences Arizona State University) for assistance with the measurements and Prof. Michael Morse (Chemistry Department, University of Utah) for the loan of a laser system.

ORCID iDs

Timothy C. Steimle https://orcid.org/0000-0002-5859-9461

References

Biscaro, C., & Cherchneff, I. 2016, A&A, 589, A132/1
Breier, A. A., Wassmuth, B., Buechling, T., et al. 2018, JMoSp, 43, 350
Brown, J. M., & Carrington, A. 2003, Rotational Spectroscopy of Diatomic Molecules (Cambridge: Cambridge Univ. Press)
Coxon, J. A., & Naxakis, S. 1985, JMoSp, 111, 102
Dagdigian, P. J., Cruse, H. W., & Zare, R. N. 1975, JChPh, 62, 1824
De Beck, E., Decin, L., Ramstedt, S., et al. 2017, A&A, 598, A53
Feng, Y., & Zhu, Z. 2019, JQSRT, 231, 37
Gobrecht, D., Cherchneff, I., Sarangi, A., Plane, J. M. C., & Bromley, S. T. 2015, A&A, 585, A6
Gomez Martin, J. C., Daly, S. M., Brooke, J. S. A., & Plane, J. M. C. 2017, CPL, 675, 56
Goto, M., Takano, S., Yamamoto, S., Ito, H., & Saito, S. 1994, CPL, 227, 287
Hansson, A., & Watson, J. K. G. 2005, JMoSp, 233, 169
Hebert, G. R., Nicholls, R. W., & Linton, C. 1980, JQSRT, 23, 229
Honjou, N. 2010, JMoSt, 939, 59
Ishizuka, S., Kimura, Y., Sakon, I., et al. 2018, NatCo, 9, 3820
Johnson, S. E., Capelle, G., & Broida, H. P. 1972, JChPh, 56, 663
Kaminski, T., Wong, K. T., Schmidt, M. R., et al. 2016, A&A, 592, A42
Kokkin, D. L., Steimle, T. C., & Demille, D. 2014, PhRvA, 90, 062503
Kraus, D., Saykally, R. J., & Bondybey, V. E. 2002, ChemPhysChem, 3, 364
Lagerqvist, A., Nilsson, N. E. L., & Barrow, R. F. 1957, Ark foer Fys, 12, 543
Launila, O., & Berg, L.-E. 2011, JMoSp, 265, 10

Lengsfield, B. H., III, & Liu, B. 1982, JChPh, 77, 6083
Linton, C., & Nicholls, R. W. 1969, JQSRT, 9, 1
Lobel, A., Bagnulo, S., Doyle, J. G., & Power, C. 2000, MNRAS, 317, 391
Partridge, H., Langhoff, S. R., Lengsfield, B. H., III, & Liu, B. 1983, JQSRT, 30, 449
Patrascu, A. T., Hill, C., Tennyson, J., & Yurchenko, S. N. 2014, JChPh, 141, 144312
Patrascu, A. T., Yurchenko, S. N., & Tennyson, J. 2015, MNRAS, 449, 3613
Reilly, N. J., Schmidt, T. W., & Kable, S. H. 2006, JPCA, 110, 12355
Saksena, M. D., Deo, M. N., Sunanda, K., Behere, S. H., & Londhe, C. T. 2008, JMoSp, 247, 47
Sarangi, A., & Cherchneff, I. 2015, A&A, 575, A95
Sato, N., Ito, H., & Kuchitsu, K. 1995, CPL, 240, 10
Takigawa, A., Kamizuka, T., Tachibana, S., & Yamamura, I. 2017, SciA, 3, eaao2149
Tenenbaum, E. D., & Ziurys, L. M. 2009, ApJL, 694, L59
Toerring, T., & Herrmann, R. 1989, MolPh, 68, 1379
Watson, J. K. G. 2008, JMoSp, 252, 5
Western, C. M. 2017, JQSRT, 186, 221
Yamada, C., Cohen, E. A., Fujitake, M., & Hirota, E. 1990, JChPh, 92, 2146
Yoshimine, M., McLean, A. D., & Liu, B. 1973, JChPh, 58, 4412
Zenouda, C., Blottiau, P., Chambaud, G., & Rosmus, P. 1999, JMoSt, 458, 61